

Response to Anonymous Referee

-The manuscript is in need of some thorough editing: there are numerous typos and poor grammar that makes the text difficult to follow at times. As mentioned below, the text describing figures is often confusing, making it difficult to determine what results are actually being shown. Many of my original comments have not been adequately addressed by the authors:

Response: We thank the reviewer for the criticisms and comments on this manuscript, which are helpful for us to further improve our presentation. We corrected all the typos and grammar mistakes that we found, and we clarified the figure captions. Our responses to the specific comments are presented below.

-I again encourage the authors not to compare to the old MMCR cloud mask. ARM's new KAZR has new processing algorithms. Therefore, the authors are comparing to the cloud mask used for the old MMCR but applied to the KAZR instead. This limits the usefulness of their results. Several times the authors mention that their method is an improvement over ARM's operation method. If the authors keep their analysis as is, statements that claim improvement over ARM's operation method need to be removed since ARM does not produce data with the MMCR algorithms applied to the KAZR.

Response: Thank the reviewer for these comment and suggestion. In the revised manuscript, we remove all statements that claim improvement over ARM's operational method and make it clear throughout the paper that the ARM algorithm that we compared with is that for MMCRs. We also make it clear that ARM's new KAZR has a new operational processing algorithm for the KAZRs at the ARM sites by adding the following paragraph at the end of section 4.1:

“It is noted that the ARM program has recently developed a new operational cloud mask algorithm for the KAZRs by applying the Hildebrand and Sekhon[1974] technique to determine the SNR values along with the spatial filter (Karen Johnson, personal communication, 2017). It is our future research task to compare our algorithm with the ARM's new operational algorithm”.

Since ARM's new algorithm still has not been published yet (Karen Johnson, personal communications), we will not compare it with ours in this paper although we are communicating with Karen for an inter-comparison of the algorithms by applying them to the same observational data.

-The authors have not made a convincing argument that the increased detection around 1.5 and 2km in Figure 7 in the cloud mask is dust. Their argument is that the MPL backscatter (what are the units for the MPL backscatter?) and depolarization is large where they detect dust with the KAZR. However, there appears to be plenty of pixels with just as large backscatter and depolarization that is not detected in the KAZR mask. To me, these KAZR detections appear to be false positives and are therefore undesirable. It would be clearer to show the PDFs of MPL aerosol backscatter and

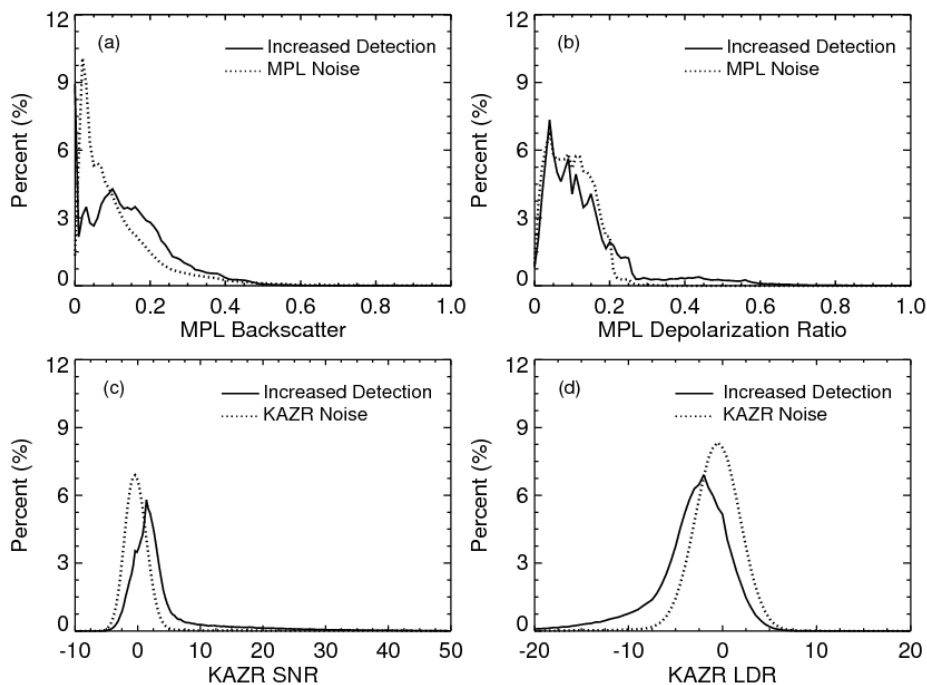
45
46
47
48

depolarization for both the pixels identified in the KAZR cloud mask and those not. If these PDFs don't differ significantly, then the authors need to revise their approach to avoid these false positives.

49 **Response:** We did not claim that the KAZR detects all features that the MPL detects
50 with large backscatter and depolarization. But it is important that the increased
51 detections are also detected by the MPL with large backscatter and depolarization,
52 indicating dust particles.

53 Following the reviewer's suggestion, we examined the PDFs of MPL aerosol
54 backscatter and depolarization corresponding to the KAZR increased feature and
55 KAZR noise regions under 3 km (See Fig. 1 below). The PDFs of MPL backscatter for
56 the KAZR feature and noise regions are quite different (Fig. 1a), with the mean
57 backscatter of 0.15 for feature and 0.10 (*photoelectrons km⁻²)/(μs μJ⁻¹)* for noise.
58 The mean of the MPL depolarization ratio is 0.16 for feature and 0.12 for noise although
59 the PDFs are more similar (Fig.1b), because dust is the main aerosol type over this
60 region. We also plot the PDFs of KAZR SNR and LDR for its feature and noise pixels
61 (Figs. 1c and 1d), which are Gaussian-like for noise pixels, very different from those
62 for the increased detections. Table 1 shows the mean values of the four quantities shown
63 in Fig.1. All the differences of these mean values between KAZR noise and increase
64 feature regions pass the significant test at 95% confidence level except for the MPL
65 depolarization ratio. These increased features from our feature mask could thus be dust
66 (or some plankton) but not the false positive.

67



68 Figure 1. PDF of (a) MPL Backscatter, (b) MPL depolarization Ratio, (c) KAZR SNR
69 and (d) KAZR LDR for the KAZR increased detections (solid line) and KAZR noise
70 (dashed line) pixels.

71

72 Table 1. Mean values of four quantities for increased KAZR feature and KAZR noise

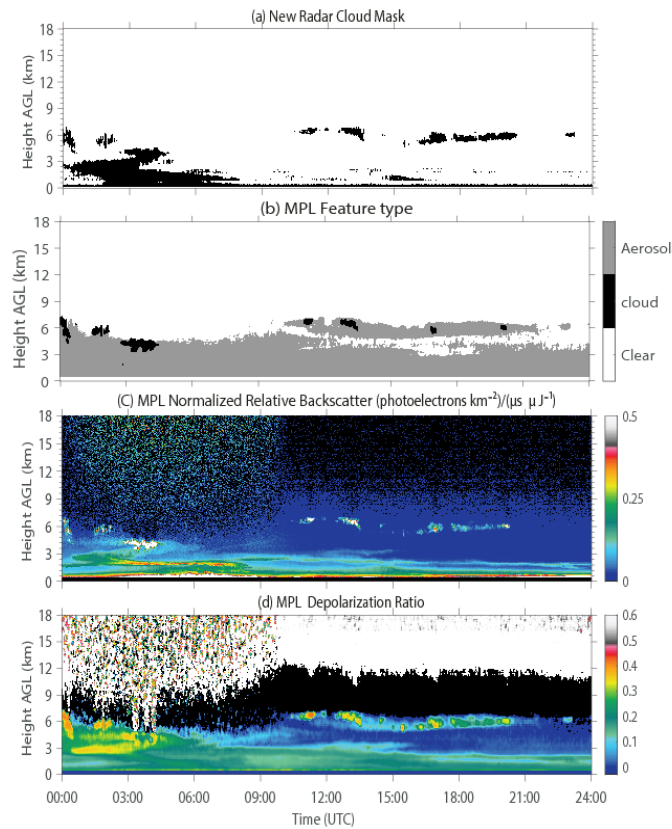
	increased KAZR feature	KAZA noise
MPL backscatter	0.15	0.10
MPL depolarization ratio	0.16	0.12
KAZR SNR	3.9	0.1
KAZR LDR	-3.0	-0.4

73

74 *-The extended comparison to the MPL is helpful for understanding the accuracy of the*
 75 *author's method. However, it appears in Figure 9 that comparisons are made to the*
 76 *MPL detection of both cloud and aerosols. In this case, any increased detection in the*
 77 *lowest several kilometers will also be detected by the MPL since aerosol is always*
 78 *present there. Above those altitudes, the results are not good with about 20% of the*
 79 *cloud mask being false positives! Figure 9 would be more useful for assessing accuracy*
 80 *if the fraction of the increased detections identified by the MPL as cloud was shown.*

81

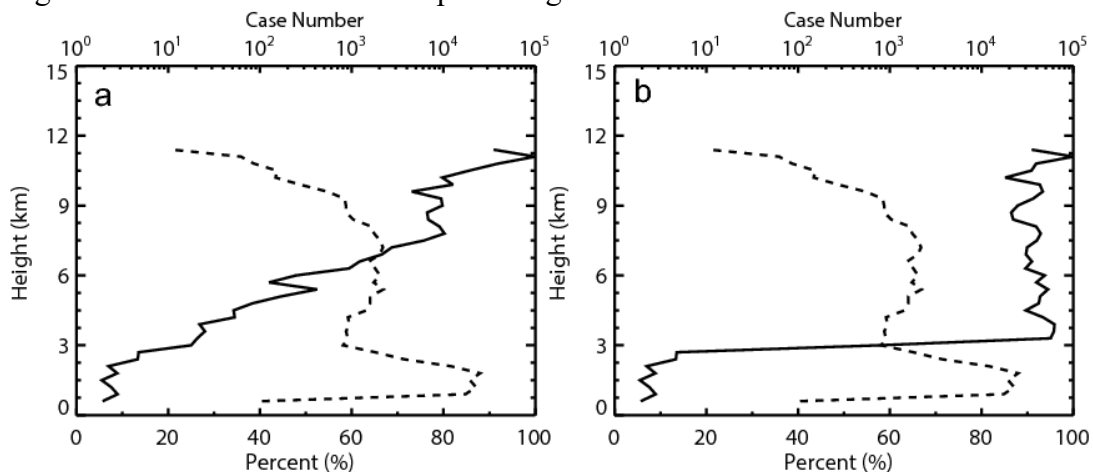
82 **Response:** Yes, we agree with the reviewer that comparing radar increased detections
 83 with clouds identified by MPL are useful. We visually looked at many cases and found
 84 that the classification of cloud and aerosol by MPL could have some issues. Figure 2
 85 shows an example. It is apparent that some signals at 6 km around 11:00-19:00 UTC,
 86 which should be clouds, are misidentified as aerosols. The MPL has a difficulty to
 87 distinguish dust from clouds (especially cirrus clouds). Unfortunately, there exist large
 88 amount of dust aerosols over the SACOL region. In any case, Fig.3a shows the
 89 percentage of the increased detections that are also detected by MPL as cloud following
 90 the review's suggestion. We can see that the percentage increases with height quickly,
 91 which are more than 80% above ~7.5 km. However, Fig.3a overall can not be used to
 92 assess our method due to the MPL feature detection issue.



93 Figure 2. The feature mask, backscatter intensity and depolarization ratio of MPL as
 94 well as the cloud radar mask on January 2, 2014. (a) Feature mask of KAZR from our
 95 method. (b) MPL feature mask. (c) MPL backscatter intensity. (d) MPL depolarization
 96 Ratio.

97

98 Figure 3. The solid lines are the percentage of the increased detections of the KAZR



99 feature mask which are also recognized by MPL. Dash lines represent the number of
 100 increased detections by our method at each height. Left is for cloud recognized by MPL,
 101 right is for both cloud and aerosol recognized by MPL.

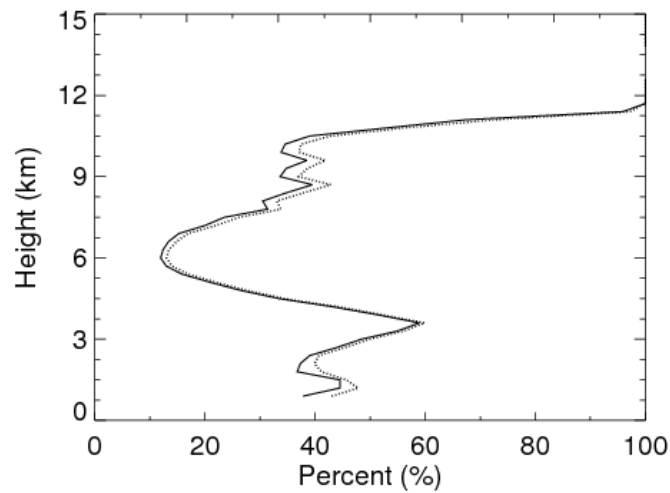
102

103 *-Figure 9 also does not show the opposite error: false negatives: i.e. detected by the*
 104 *MPL but not the KAZR cloud mask. In lieu of Figure 9 it would be more helpful to just*
 105 *show a confusion matrix (similar to what the authors present in Table 1) for the MPL*

106 cloud mask compared to both the KAZR cloud mask both with and without the noise
 107 reduction step. That way the change in both error rates could be assessed.

108

109 **Response:** Figure 4 shows the profile of false negative (i.e. the percentage of the cloud
 110 pixels identified by MPL but not by KAZR in the total MPL detected cloud pixels). We
 111 can see that our method with the noise reduction has relative smaller false negatives
 112 especially in the layers under 3 km and between 7 and 10 km. Table 2 is the confusion
 113 matrix of the MPL detection and the KAZR mask. Overall, 71% feature mask identified
 114 by MPL also recognized by the new method, while this percent is 69% for the algorithm
 115 without noise reduction. The difference of false positive between two method is only



116 0.1% (table 2).

117 Figure 4. The percentage of the cloud pixels identified by MPL but not by KAZR in the
 118 total MPL detected cloud pixels. Solid line represents for the algorithm with noise
 119 reduction step. Dot line is for the method without noise reduction scheme.

120

121 Table 2. The confusion matrix of KAZR feature mask results from both our and old
 122 methods estimated by MPL

	our method	old method
True Positive	70.7%	68.9%
True Negative	95.4%	95.5%
False Positive	4.6%	4.5%
False Negative	29.3%	31.1%

123

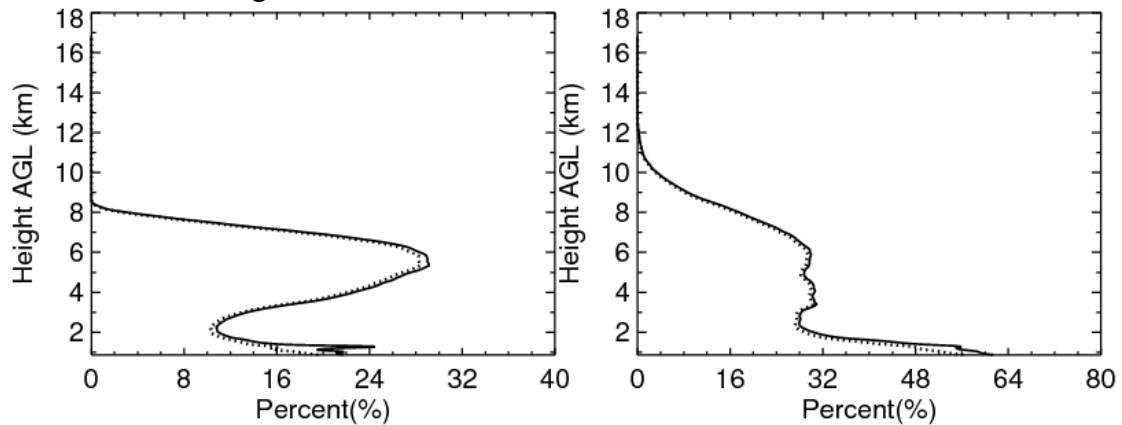
124

125 *-I cannot tell the line styles apart in the top panel of Figure 8. I'm also unsure what is*
 126 *being plotted there as the caption mentions a "confusion matrix" but no matrix is given.*
 127 *It is also not clear what the lines in the bottom panels of Figure 8 are normalized to. It*
 128 *would be most useful to show the comparison of cloud occurrence profiles (i.e. number*
 129 *of cloudy pixels /total number of pixels), but that doesn't appear to be what is plotted*

130 here.

131

132 **Response:** Figure 8 in our manuscript is replaced with a new one. We plotted cloud
133 occurrence profiles to demonstrate cloud vertical distributions detected with and
134 without noise reduction scheme in Figure 5 as the reviewer suggested. Overall, more
135 than 5.3% cloud pixels are detected by our method comparing with the old MMCR
136 algorithm. We don't replace Figure 8 in our paper with this one, since the main purpose
137 of this paper is to show the ability of our algorithm on recognizing weak signals. It is
138 more clear to compare the increased detection just with the old method. The lines in the
139 bottom panels of Figure 8 are normalized to the number of feature identified by MMCR
140 method in each height interval.



141 Figure 5. Cloud occurrence profiles for the feature detection algorithm with and without
142 noise reduction step. Left panel is for December,2013 and January, February and March,
143 2014. Right panel is for June, July and August 2014.

1 An Improved Hydrometeor Detection Method for Millimeter-Wavelength Cloud

2 Radar

3 Ge Jinming¹, Zhu Zeen¹, Zheng Chuang¹, Xie Hailing¹, Zhou Tian¹, Huang Jianping¹,

4 and Fu Qiang^{1,2}

5 ¹Key Laboratory for Semi-Arid Climate Change of the Ministry of Education and

6 College of Atmospheric Sciences, Lanzhou University, Lanzhou, 730000, PRC

7 ²Department of Atmospheric Sciences, University of Washington, Seattle, WA,

8 98105, USA

9

10

11

12

13

14

15

16

17

18

19

20

Submitted to *Atmos. Chem. and Phys.*

21

qfu@atmos.washington.edu

22

~~December~~May 6, 2016

Abstract

A ~~new~~modified method with a new noise reduction scheme that can reduce the noise distribution to a narrow range is proposed to distinguish clouds and other hydrometeors from noise and recognize more features with weak signal –in cloud radar observations. ~~A noise reduction scheme that can reduce the noise distribution to a narrow range is proposed in our method in order to recognize more weak signal clouds.~~ A spatial filter with central weighting, which is widely used in ~~current~~ cloud radar hydrometeor detection algorithms, is also involved in our method to examine radar return for significant levels of signals. “Square clouds” were constructed to test the ~~two~~ our algorithm and the method used for the U.S. Department of Energy Atmospheric Radiation Measurements program millimeter-wavelength cloud radar. We also applied ~~our both the methods~~ to six months of cloud radar observations at the Semi-Arid Climate and Environment Observatory of Lanzhou University and compared the results with those obtained by applying the U.S. Department of Energy (DOE) Atmospheric Radiation Measurements (ARM) program operational algorithm. It was found that our method has significant advantages in recognizing clouds with weak signal and reducing the rates of both failed negative and false positive hydrometeor identifications in simulated clouds.

41 1. Introduction

42 Clouds, which are composed of liquid water droplets, ice crystals or both, cover
43 about two-thirds of the earth surface at any time [e.g., *King et al.*, 2013]. By reflecting
44 solar radiation back to the space (the albedo effect) and trapping thermal radiation
45 emitted by the Earth surface and the lower troposphere (the greenhouse effect), clouds
46 strongly modulate the radiative energy budget in the climate system [e.g., *Qiang Fu et*
47 *al.*, 2002; *Huang et al.*, 2007; *Huang et al.*, 2006a; *Huang et al.*, 2006b; *Ramanathan*
48 *et al.*, 1989; *Su et al.*, 2008]. Clouds are also a vital component of water cycle by
49 connecting the water-vapor condensation and precipitation. Despite the importance of
50 clouds in the climate system, they are difficult to represent in climate models [e.g.,
51 *Williams and Webb*, 2009], which causes the largest uncertainty in the predictions of
52 climate change by general circulation models (GCMs) [e.g., *Randall*, 2007; *Stephens*,
53 2005; *Williams and Webb*, 2009].

54 Cloud formation, evolution and distribution are governed by complex physical and
55 dynamical processes on a wide range of scales from synoptic motions to turbulence
56 [*Bony et al.*, 2015]. Unfortunately, the processes that occur on smaller spatial scales
57 than a GCM grid box cannot be resolved by current climate models, and the coupling
58 between large scale fluctuations and cloud microphysical processes are not well
59 understood [e.g., *Huang et al.*, 2006b; *Mace et al.*, 1998; *Yan et al.*, 2015; *Yuan et al.*,
60 2006]. Moreover, the cloud horizontal inhomogeneity and vertical overlap are not
61 resolved by GCMs [*Barker*, 2000; *Barker and Fu*, 2000; *Q. Fu et al.*, 2000a; *Q. Fu et*
62 *al.*, 2000b; *Huang et al.*, 2005; *Li et al.*, 2015]. To better understand cloud processes

63 for improving their parameterization in climate models and revealing their evolution in
64 response to climate change, long-term continuous observations of cloud fields in terms
65 of both macro- and micro-physical properties are essential [e.g., *Ackerman and Stokes,*
66 *2003; Sassen and Benson, 2001; Thorsen et al., 2011; Wang and Sassen, 2001*].

67 Millimeter-wavelength Cloud Radars (MMCRs) can resolve cloud vertical structure
68 for their occurrences and microphysical properties [e.g., *Clothiaux et al., 1995; Kollias*
69 *et al., 2007a; Mace et al., 2001*]. The wavelengths of MMCRs are shorter than those of
70 weather radars making them sensitivity to cloud droplets and ice crystals and can
71 penetrate multiple cloud layers [e.g., *Kollias et al., 2007a*]. Because of their outstanding
72 advantages for cloud research, millimeter-wavelength radars have been deployed on
73 various research platforms including the first space-borne millimeter-wavelength Cloud
74 Profiling Radar (CPR) onboard the CloudSat [*Stephens et al., 2002*]. Ground-based
75 cloud radar are operated at the U.S. Department of Energy's Atmospheric Radiation
76 Program (ARM) observational sites (used to be MMCRs, now are replaced with a new
77 generation of Ka band Zenith Radar (KAZR)) [e.g., *Ackerman and Stokes, 2003;*
78 *Clothiaux et al., 2000; Clothiaux et al., 1999; Kollias et al., 2007b; Protat et al., 2011*]
79 and in Europe [*Illingworth et al., 2007; Protat et al., 2009*]. In July 2013, a KAZR was
80 deployed in China at the Semi-Arid Climate and Environment Observatory of Lanzhou
81 University (SACOL) site (latitude: 35.946°N; longitude: 104.137°E; altitude: 1.97 km)
82 [*Huang et al., 2008*], providing an opportunity to observe and reveal the detailed
83 structure and process of the mid-latitude clouds over the semi-arid regions of East Asia
84 semi-arid regions.

85 Before characterizing the cloud physical properties from the cloud radar return signal,
86 we first need to distinguish and extract the hydrometeor signals from the background
87 noise (i.e. cloud mask). A classical cloud mask method was developed in Clothiaux et
88 al.[2000; 1995] by analyzing the strength and significance of returned signals. This
89 method consists of two main steps. First any power in a range gate that is greater than
90 a mean value of noise plus one standard deviation is selected as a bin containing
91 potential hydrometer signal. Second, a spatial-time coherent filter is created to estimate
92 the significance level of the potential hydrometer bin signal to be real. This cloud mask
93 algorithm is operationally used for the ARM MMCRs data analysis and was later
94 adopted to the CPR onboard the CloudSat [*Marchand et al.*, 2008].

95 It is recognized that by visually examining a cloud radar return image, one can easily
96 tell where the return power is likely to be caused by hydrometeors and where the power
97 is just from noise. This ability of human eye on extracting and analyzing information
98 from an image has been broadly studied in image processing and computer vision, ~~and~~
99 ~~a~~A number of mathematical methods for acquiring and processing information from
100 images have been developed, including some novel algorithms for noise reduction and
101 edge detection [*Canny*, 1986; *He et al.*, 2013; *Marr and Hildreth*, 1980; *Perona and*
102 *Malik*, 1990]. In this paper, we ~~propose a modified~~develop a new cloud mask method
103 for cloud radar by noticing that removing noise from signal and identifying cloud
104 boundaries are the essential goals of cloud mask. This method reduces the radar noise
105 while preserving cloud edges by employing the bilateral filtering that is widely used in
106 the image processing [*Tomasi and Manduchi*, 1998]. The power weighting probability

107 method proposed by Marchand et al.[2008] is also adopted in our method to prevent
108 the cloud corners from being removed. It is found that our improved hydrometeor
109 detection algorithm is ~~more~~ efficient in terms of reducing false positives and negatives
110 as well as identifying cloud features with weak signals such as thin cirrus clouds.

111 The KAZR deployed at the SACOL is described in section 2 and the ~~modified new~~
112 cloud mask algorithm is introduced in section 3. The applications of the new scheme to
113 both hypothetical and observed cloud fields including a comparison with previous
114 schemes are shown in section 4. Summary and conclusions are given in section 5.

115 2. The KAZR Radar

116 The SACOL KAZR, built by ProSensing Inc. of Amherst, MA, is a zenith-pointing
117 cloud radar operating at approximately 35 GHz for the dual-polarization measurements
118 of Doppler spectra. The main purpose of the KAZR is to provide vertical profiles of
119 clouds by measuring the first three Doppler moments: reflectivity, radial Doppler
120 velocity, and spectra width. The linear depolarization ratio [Marr and Hildreth, 1980]
121 can be computed from the ratio of cross-polarized reflectivity to co-polarized
122 reflectivity.

123 The SACOL KAZR has a transmitter with a peak power of 2.2 kw and two modes
124 working at separate frequencies. One is called “chirp” mode that uses a linear-FM
125 (frequency modulation) pulse compression to achieve high radar sensitivity of about -
126 65 dBZ at 5 km altitude. The minimum altitude (or range) that can be detected in chirp
127 mode is approximately 1 km AGL. To view clouds below 1 km, a short pulse or “burst
128 mode” pulse is transmitted at a separate frequency just after transmission of the chirp

129 pulse. This burst mode pulse allows clouds as low as 200 m to be measured. The chirp
130 pulse is transmitted at 34.890 GHz while the burst pulse is transmitted at 34.830 GHz.
131 These two waveforms are separated in the receiver and processed separately.

132 The pulse length is approximately 300 ns (giving a range resolution of 45 m), while
133 the digital receiver samples the return signal every 30 m. The interpulse period is 208.8
134 μ s, the number of coherent averages is 1, and the number of the fast Fourier transform
135 (FFT) points is currently set to 512. An unambiguous range is thus 31.29 km, an
136 unambiguous velocity is 10.29 m/s, and a velocity resolution σ_v is 0.04m/s. The signal
137 dwell time is 4.27s. These operational parameters are set for the purpose of having
138 enough radar sensitivity and accurately acquiring reflectivities of hydrometeors. In this
139 study, we mainly use radar observed reflectivity (dBZ) data to test our new hydrometeor
140 detection method.

141 3. Hydrometeor detection algorithm

142 The basic assumption in the former cloud mask algorithms [e.g., *Clothiaux et al.*,
143 1995; *Marchand et al.*, 2008] is that the random noise power follows the normal
144 distribution. ~~In this study, several~~Here clear sky cases in all seasons from the KAZR
145 observations were firstly ~~selected to analyzed for~~ its background noise power
146 distributions ~~(Fig.1). As demonstrated in Fig.1a for~~Figure 1a shows an example of a
147 clear-sky case during 0000 to 1200 UTC on January 21st, 2014, ~~. The noise power is~~
148 estimated from the top 30 range gates, which includes both internal and external
149 sources~~[Fukao and Hamazu, 2014], [Fukao and Hamazu, 2014]. It~~ has an apparent non-
150 Gaussian distribution with a positive skewness of 1.40 (Fig.1a). The signal-to-noise

151 ratio (SNR) is defined as:

$$152 \quad \text{SNR} = 10\log\left(\frac{P_s}{P_n}\right) \quad (1)$$

153 where P_s is the power received at each range gate in a profile, P_n is the mean noise
154 power that is estimated by averaging the return power in the top 30 range gates which
155 are between 16.8 and 17.7 km AGL. Since this layer is well above the tropopause, few
156 atmospheric hydrometeors existing in this layer can scatter enough power back to
157 achieve the radar sensitivity. Figure 1a shows that the SNRs for clear skies closely
158 follow a Gaussian distribution. Instead of using radar received power, the SNR is used
159 ~~to estimate~~ the input in our cloud mask algorithm including estimating the
160 background noise level. This is because ~~and taken as the input to the cloud mask~~
161 ~~procedure since the SNR satisfies the assumption of a normally distributed noise and in~~
162 our method the chance for ~~the a~~ central range gate to be a noise or a potential signal
163 feature, relies on ~~calculating~~ the probability for a given range of SNR values based
164 on following the Gaussian distribution. Note that the mean value of the SNR for the
165 noise power is not zero, but a small negative value of about -0.3. This is because the
166 mean of the noise power is larger than its the median due to its positive skewed
167 distribution. It is further noted that for the noise the distribution of SNR and its mean
168 for the top 30 range gates are the same as those from the lower atmosphere.

169 The SNR value is treated as the brightness of a pixel in an image $f(x, y)$ in our
170 hydrometeor detection method. In an image processing, the random noise can be
171 smoothed out by using a low pass filter, which gives a new value for a pixel of an image
172 by averaging with neighboring pixels [Tomasi and Manduchi, 1998]. The cloud signals

173 are highly correlated in both space and time and have more similar values in near pixels
174 while the random noise values are not correlated. ~~Therefore, as illustrated in Figure. 2a~~
175 ~~shows, a schematic comparison of the original noise, reduced noise and hydrometeor~~
176 ~~signal distributions: this-the~~ low pass filter ~~can-could~~ efficiently reduce the original
177 radar noise represented by the green line to a narrow bandwidth (blue line) while
178 keeping the signal preserved. By reducing the standard deviations of noise, which
179 shrinks the overlap region of signal and noise and enhances their contrast, the weak
180 signals (yellow area) that cannot be detected based on original noise level may become
181 distinguished.

182 ~~Based on~~ Following this idea, we develop a non-iterative hydrometeor detection
183 algorithm by applying a noise reduction and a central pixel weighting schemes. Figure
184 3 shows the schematic flow diagram of our method. For given mean SNR values (S_o)
185 and one standard deviation (σ_o) of the original background noise, ~~the~~ input SNR data
186 set is first separated into two groups. One group with values greater than ~~the mean~~
187 ~~background noise- $S_o + 3\sigma_o$ -SNR (S_o) plus three times of its standard deviation (σ_o)~~
188 are considered as the cloud features that can be confidently identified. Another group
189 with values between S_o and $S_o + 3\sigma_o$ may potentially contain moderate ($S_o + \sigma_o <$
190 $SNR \leq S_o + 3\sigma_o$) to weak ($S_o < SNR \leq S_o + \sigma_o$) cloud signals, which will further go
191 through a noise reduction process. Here S_o and σ_o are estimated from the top 30
192 range gates of each five successive profiles.

193 The noise reduction process is ~~mainly~~ performed by convolving radar SNR time-
194 height data with a low pass filter. The Gaussian Filter, which outputs a `weighted

195 average' of each pixel and its neighborhood with the average weighted more towards
196 the value of the central pixel (v_0), is one of the most common functions of the noise
197 reduction filter. A 2-D Gaussian distribution kernel, shown in Fig. 2b₁, can be expressed
198 as:

$$199 \quad G(i, j) = \frac{1}{2\pi\sigma^2} \exp\left(-\frac{i^2+j^2}{2\sigma^2}\right) \quad (2)$$

200 where i and j are the indexes in a filter window which are 0 for the central pixel, and σ
201 is standard deviation of the Gaussian distribution for the window size of the kernel.
202 Equation (2) is used in our study to filter the radar SNR image. Note that the
203 convolution kernel is truncated at about three standard deviations away from the mean
204 in order to accurately represent the Gaussian distribution. Figure 1b are the cumulative
205 distribution functions (CDFs) of clear sky SNR by convolving the same data in Fig. 1a
206 with ~~four~~ filters that have different kernel sizes (3×3 , 5×5 , 7×7 and 9×9 pixels)
207 corresponding to the σ ranging from 0.5 to 2. The original SNR values are distributed
208 from about -5 to 5. After convolving the image with the Gaussian filter, the SNR
209 distribution can be constrained to a much narrower range. It is clear that the filter with
210 a larger kernel size is more effective in suppressing the noise. Shown in Fig. 1c are
211 results for a cloudy case on January 4th, 2014 by applying the filter to the range gates
212 inside the cloud but adjacent to the boundary. ~~It is showing~~ that a larger kernel size
213 shifts the SNR farther away from the noise region. It therefore appears that increasing
214 the standard deviation (i.e. the window size) ~~continues would~~ reducing the noise and
215 ~~increasing enhance~~ the contrast between signal and noise more effectively. At the same
216 ~~time~~ On the other hand, however, a larger kernel can also attenuate or blur the high

217 frequency components of an image (e.g., the boundary of clouds) more ~~at the same time~~.

218 As shown in Fig. 1d, when the window size is increased from 3×3 ($\sigma=0.5$) to 9×9 ($\sigma=2$),

219 the SNR distribution of the range gates that are outside the cloud but adjacent to the

220 boundary gradually move toward ~~larges-larger~~ values. This will consequently raise the

221 risk of misidentifying cloud boundaries. To solve this problem, a bilateral filtering idea

222 proposed by *Tomasi and Manduchi* [1998] is adopted here. Considering a sharp edge

223 between cloudy and clear region as shown in Fig. 2b₂, we define a $\delta(i, j)$ function that

224 when the central pixel is on the cloudy or clear side, gives a weighting of 1 to the similar

225 neighboring pixels (i.e. on the same side), and 0 to the other side. After combining this

226 δ function to the Gaussian kernel in Fig. 2b₁, we can get a new non-linear function

227 called bilateral kernel as shown in Fig. 2b₃. It can be written as:

$$228 \quad B(i, j) = \frac{1}{2\pi\sigma^2} \exp\left(-\frac{i^2+j^2}{2\sigma^2}\right) \cdot \delta(i, j). \quad (3)$$

229 Thus the bilateral kernel will reduce averaging noises with signals, and vice versa. The

230 noise-reduced image $h(x, y)$ is produced by convolving the bilateral kernel with the

231 ~~original~~ input image $f(x, y)$ as:

$$232 \quad h(x, y) = k^{-1}(x, y) \sum_{j=-w}^{j=w} \sum_{i=-w}^{i=w} f(x + i, y + j) \cdot B(i, j) \quad (4)$$

233 where $\pm w$ is the bounds of the finite filter window, $k^{-1}(x, y)$ is defined as

234 $1 / \sum_{j=-w}^{j=w} \sum_{i=-w}^{i=w} B(i, j)$ which is used to normalize the weighting ~~coefficients~~. Since

235 the bilateral kernel function only average the central pixel with neighbors on the same

236 side (Fig. 2b), ideally it will preserve sharp edges of a target. We will discuss how to

237 construct the δ function in order to group the central pixel with its neighbors later in

238 this section. In the noise reduction process, a 5×5 window size (i.e., 25 bins in total) is

239 specified for the low pass filter, which is empirically determined by visually comparing
240 the cloud masks with original images. We should keep in mind that ~~the window size is~~
241 ~~compromised since~~ a small window size is less effective in noise reduction but a large
242 window is not suitable for recognizing weak signals.

243 For performing the noise reduction with Eq. (4) in a 5x5 filter window, the number
244 of range bins (N_s) with signal greater than $S_o + 3\sigma_o$ are first counted. These N_s range
245 bins are then subtracted from the total 25 of the range bins in the filter window. Note
246 that a noise reduction is only applied when the central pixel is among the 25- N_s bins,
247 and the δ function is set to be zero for the N_s range bins. If the remaining 25- N_s range
248 bins are all noises, the range bin number (N_m) with SNR greater than $S_o + \sigma_o$ should
249 be about equal to an integral number (N_t) of $0.16 \times (25 - N_s)$ where 0.16 is the probability
250 for a remaining range bin to have a value greater than $S_o + \sigma_o$ for a Gaussian noise.
251 Thus when N_m is equal to or smaller than N_t , all the 25- N_s range bins could only
252 contain pure noise and/or some weak cloud signals. In this case, the δ function is set
253 to 1 for all the 25- N_s bins. When N_m is found to be larger than N_t , the 25- N_s range
254 bins might contain a combination of moderate signal, noise and/or some weak clouds.
255 In this case, $S_o + \sigma_o$ is selected as a threshold to determine whether the ~~neighboring~~
256 pixels are on the same side of the central pixel. If the central pixel has a value greater
257 than $S_o + \sigma_o$, the δ function is assigned to 1 for the 25- N_s pixels with $\text{SNR} \geq S_o +$
258 σ_o , but 0 for the ~~neighboring~~ bins with $\text{SNR} < S_o + \sigma_o$. If the central pixel is less than
259 $S_o + \sigma_o$, the δ function is assigned to 1 for the ~~neighboring~~ pixels with $\text{SNR} < S_o +$
260 σ_o , but 0 for the 25- N_s bins with $\text{SNR} \geq S_o + \sigma_o$.

261 After picking out the strong return signals and applying the noise reduction scheme,
 262 the new background noise S_n and its standard deviation σ_n are estimated. While S_n is
 263 the same as S_o , the σ_n is significantly reduced, which is a half of σ_o . This will make
 264 it possible to identify more hydrometeors as exhibited in Fig.2a. We assign different
 265 confidence level values (which is called the mask value in this study) to the following
 266 initial cloud mask according to the SNR. 40 is first assigned to the mask of any range
 267 bins with $SNR > S_o + 3\sigma_o$ in the original input data. For the rest of the range bins
 268 after applying the noise reduction, if the $SNR > S_n + 3\sigma_n$, the mask is assigned to be
 269 30; if $S_n + 2\sigma_n < SNR \leq S_n + 3\sigma_n$, the mask is 20; if $S_n + \sigma_n < SNR \leq S_n + 2\sigma_n$,
 270 the mask is 10; and the remaining range bin mask is assigned to be 0. Thus, a mask
 271 value assigned to a pixel represents the confident level for the pixel to be a feature.

272 To reduce both false positives (i.e. false detections) and false negatives (i.e. failed
 273 detections), the next step is to estimate whether a range gate contains significant
 274 hydrometeor. Following Clothiaux et al.[2000; 1995] and Marchand et al.[2008], a 5×5
 275 spatial filter is used to calculate the probability of clouds and noise occurring in the 25
 276 range gates. The probability of central pixel weighting scheme proposed by Marchand
 277 et al. [2008] is adopted here, and the weighting for the central pixel is assigned
 278 according to its initial mask value. The probability is calculated by

$$279 \quad p = G(L)(0.16^{N_T})(0.84^{N_0}) \quad (5)$$

280 where N_0 is the number of masks with zero masks values, N_T is the number of masks
 281 with non-zeros mask values and $N_0 + N_T = 25$; $G(L)$ is the weighting probability of
 282 the central pixel that could be a false detection at a given where L is the significant level

283 of L (i.e., mask value) in the initial cloud mask. Here $\{G(0)=0.84, G(10)=0.16,$
 284 $G(20)=0.028, G(\geq 30)=0.002\}$. If p estimated from Eq. (5) is less than a given threshold
 285 (p_{thresh}), then the central pixel is likely to be a hydrometeor signal. The cloud mask
 286 ~~value in the cloud mask~~ will be set to ~~be~~ the same value as in the initial mask if it is
 287 non-zero; otherwise it will be set to 10. Likewise, if $p > p_{thresh}$, then the central pixel
 288 is likely to be noise and the mask value will be set to 0. This process is iterated 5 times
 289 for each pixel to obtain the final cloud mask.

290 Following Marchand et al. [2008] who well explained the logic of choosing a proper
 291 threshold, p_{thresh} is calculated as

$$292 \quad p_{thresh} = (0.16^{N_{thresh}})(0.84^{25-N_{thresh}}) \quad (6)$$

293 Note that a smaller p_{thresh} will keep the false positives lower but increase the false
 294 negative. Herein we adopt the p_{thresh} of 5.0×10^{-12} used in Clothiaux et al.[2000], which
 295 is approximately equivalent to $N_{thresh} = 13$, ~~is selected~~.

296 Figure 4 illustrate the main steps of our detection method by using the data from
 297 January 8th, 2014. Figure 4a is the original SNR input. Figure 4b shows the SNR
 298 distribution after the noise reduction process. One can see that the SNR after being
 299 compressed to a narrow range ~~and~~, becomes much smoother than original input, ~~after~~
 300 ~~the noise reduction process~~. This step significantly increases the contrast between signal
 301 and noise. Figure 4c indicates the range gates that potentially contain hydrometeors
 302 in the initial cloud mask. Figure 4d is the final result by applying the spatial filter.

303 4. Results

304 4.1 Detection test

305 To test the performance of our hydrometeor detection method, we create 7 squares
306 of SNR with sides of 100, 50, 25, 15, 10, 5, and 3 bins to mimic the radar “time-height”
307 observations as shown in Fig. 5. The background noise is randomly given by a Gaussian
308 distribution with a mean S_0 and a standard deviation σ_0 . The targets in panels a₁, a₂
309 and a₃ are set with different SNR values to represent situations in which clouds have
310 strong, moderate and weak signals, respectively. In panel a₁, the targets signals are set
311 to be $S_0 + 10\sigma_0$. In panel a₂, the targets signals distribute from $S_0 + \sigma_0$ to $S_0 + 3\sigma_0$
312 with a mean value of $S_0 + 2\sigma_0$. In panel a₃, the targets SNRs range from S_0 to $S_0 +$
313 σ_0 with a mean value of $S_0 + 0.5\sigma_0$.

314 The three middle panels in Fig. 5 show the results after applying the noise reduction.
315 Again, Comparing with the input signals, we can see that the background noise is well
316 compressed and becomes ~~more smooth~~smoother. The shapes of the square targets are
317 all well maintained with sharp boundaries for strong and moderate signals (see Fig.5
318 ~~panels b1 and b2~~). In ~~panel Fig.5 b3~~ for weak signals, the 3-bin square target is not
319 obvious while the other 6 squares are still distinguishable. To separate the compressed
320 background noise from hydrometeor signals, the 5×5 spatial filter is further applied to
321 the noise-reduced data. The three right panels in Fig.5 show the final mask results.
322 Generally, the hydrometeor detection method can identify those targets well. Six of the
323 seven square targets can be identified for clouds with strong and moderate SNR. The
324 3×3 square is missed because the small targets cannot be resolved by the 5×5 spatial
325 filter. Since the temporal resolution of KAZR is about 4 seconds, we expect that a cloud
326 only having 3 bins in horizontal would be rare. For the targets with weak SNR values,

327 the 3×3 and 5×5 square targets are missed, but the rest five square targets are
328 successfully distinguished and their boundaries are well maintained.

329 To further demonstrate the performance of our method ~~to~~for detecting the
330 hypothetical clouds in Fig.5 a1, a2, and a3, the false and failed detection rates are listed
331 in the table 1. For strong signals, no background noise pixel is misidentified as one
332 containing hydrometeors at level 40. Although at levels less than 40, some noise pixels
333 around the edges of targets are identified as signals, the false detection is within 0.05%.
334 The failed detection rate is about 0.24%. For moderate signals, the failed detection rate
335 is still as small as 0.23%, while the false detection increases a little to 0.10% at the
336 confidence levels below 30. The failed detection can reach up to 9.77% for weak signal
337 at level 10, but more than 90% weak signals can be captured in our method. Note that
338 the false positive is less than 0.01%; in other words, any range gate that is detected
339 likely as a signal bin will have extremely high likelihood to contain hydrometeors.

340 The simple square clouds are also tested by using the ARM ~~operational~~hydrometeor
341 detection algorithm developed for the MMCRs [Clothiaux *et al.*, 2000; 1995] ~~that~~
342 which does not include the noise reduction and weighting schemes. As can be seen in
343 Fig. 6, ~~this ARM-operational~~ algorithm can only find five of the seven square targets
344 with strong and moderate SNR. Meanwhile without central pixel weighting, the corners
345 of the targets become rounded and more than 2.23% of hydrometeors are missed for
346 strong and moderate cloud cases. ~~Without the noise reduction~~More importantly, none
347 of the weak cloud signals can be detected. Comparing Fig.5 and Fig.6, it is obvious that
348 our hydrometeor detection method can well maintain the cloud boundary, keep both

349 false and failed detection rate as low as a few percent for strong and moderate cloud
350 cases, and has a remarkable advantage in recognizing weak signals.

351 It is noted that the ARM program has recently developed a new operational cloud
352 mask algorithm for the KAZRs by applying the Hildebrand and Sekhon [1974]
353 technique to determine the SNR values along with the spatial filter (Karen Johnson,
354 personal communication, 2017). It is our future research task to compare our algorithm
355 with the ARM's new operational algorithm.

356 4.2 Application to the SACOL KAZR observations

357 Our hydrometeor detection method was then applied to the winter and summer
358 months (Dec. in 2013, Jan., Feb., Jun., Jul. and Aug. in 2014) KAZR data at the SACOL.
359 A micropulse lidar (MPL) transmitted at 527 nm is operated nearby the KAZR. Lidar
360 is more sensitive to thin cirrus clouds and thus used to assess the performance of our
361 algorithm. Figure 7 a, b & c show an one-day example of radar reflectivity, normalized
362 backscatter and depolarization ratio of lidar, respectively. The cloud masks from our
363 detection method and the ARM ~~operational MMCR~~ method ~~without the noise reduction~~
364 ~~and the central pixel weighting~~ are shown in Fig. 7d&e. The MPL feature mask is
365 derived by modifying the method ~~proposed~~ developed in Thorsen et al. [2015] and
366 Thorsen and Fu [2015] (~~see is shown in~~ Fig. 7f). The vertical and horizontal resolutions
367 of the radar and lidar are different, and we map the observed data and derived feature
368 mask on the same height and time coordinates for ~~a simple~~ the purpose of a comparison.
369 A distinct thin feature layer appears at about 8 km during 1500 to 1830 UTC from the
370 lidar observation which is clearly identified as a cirrus cloud using the depolarization

371 ratio. The contrast between the cirrus layer and background from the KAZR observation
372 (Fig. 7a) is very weak, and only a few range gates are identified as the ~~ones containing~~
373 hydrometeors using the method without the noise reduction and weighting (Fig. 7d).
374 However, our cloud mask method can find more range gates (about 2.8 times of ARM's
375 result). All these increased range bins from our method are also detected as thin cirrus
376 by the MPL (Fig. 7f). Another apparent discrepancy exists in the low atmosphere layer.
377 A non-negligible number of range gates at about 2 km are recognized as hydrometeor
378 echoes by our method but mostly missed by former technique. This feature layer is also
379 apparent in lidar observations with both relative large backscatter intensities and
380 depolarization ratios(Fig. 7b&c). MPL recognizes this feature as an aerosol layer. ~~In~~
381 From our KAZR observations, we did find some dust events that were detected by this
382 millimeter wavelength radar (see the auxiliary Fig.1). Those ~~hydrometeor-feature~~
383 echoes detected by our method might partly be caused by large dust particles. Although
384 the dust is not desired for cloud mask, the appearance of those particles dose prove the
385 ability of our method on recognizing weak signals.

386 The upper two panels in Fig. 8 compares the number of occurrences of the detected
387 hydrometeor range bins from our ~~new~~ methods with that from the ARM ~~operational~~
388 MMCR algorithm for the six months of data. Generally, one can see that the variations
389 of the identified hydrometeor numbers with height from the two techniques are in a
390 good agreement. The distinct discrepancies appear at about 2 km in Winter and above
391 13 km in Summer where our method apparently identify more hydrometeors. To
392 illustrate the improvements of our method and quantitatively evaluate the two schemes

393 used in the algorithm, we plot the percent change of the detected hydrometeor bins from
394 our method comparing with that from the ARM MMCR ~~operational~~ method in the
395 lower two panels in Fig. 8. As expected from the results in the test square clouds, our
396 method can identify more signals. The remarkable feature is that the increased
397 percentage is over 20% at high altitude, indicating that our method can recognize more
398 cirrus clouds. The increased percentage of hydrometeor derived only with the weighting
399 scheme (dashed line) and with both the noise reduction and weighting schemes (solid
400 line) are separated to demonstrate the individual contribution of the scheme to the
401 improvement of our method. In ~~winter~~, winter, the number of the detected hydrometeors
402 only with the weighting scheme is almost the same as that from the ARM ~~operational~~
403 method at layer from 3.5 to 9 km AGL, while this number will increase by about 5% if
404 the noise reduction scheme is involved, indicating that some hydrometeors with weak
405 SNR values may exist in this layer. Above and below this atmospheric layer, the
406 increased percentage is largely determined by the weighting scheme. In summer, the
407 two lines s almost overlap each other between 3.5 and 9.5 km with values below 5%,
408 revealing that the bins found by our method in the middle atmospheric layer are mainly
409 around the boundaries of clouds. We may infer that in summer season, clouds in middle
410 level are usually composed of large droplets with strong SNR values. The two lines are
411 gradually apart with height. This is because hydrometeors in the upper ~~of~~ troposphere
412 ~~are~~ usually with have smaller size ~~and that~~ causes s weak SNR values, which ~~that~~ will be
413 effectively detected by the noise reduction scheme. ~~Note that the confusion matrix~~
414 ~~shows that the cancellation errors can be negligible.~~

415 We also analyzed ~~the data in January–July, 2014~~ when both KAZR and MPL
416 observations are available, ~~and compared our KAZR cloud mask with MPL feature~~
417 ~~detection. Figure 9a and showed~~ the percentage of the increased detections identified
418 by both KAZR with our method and MPL observations as ~~compared~~ normalized to the
419 KAZR total increased detections in Fig. 9. Here we should point out that MPL has a
420 difficulty to distinguish dust from clouds (especially cirrus clouds). Unfortunately,
421 there exist large amount of dust aerosols over the SACOL region. We visually looked
422 at many cases and found many MPL signals, which should be clouds, are misidentified
423 as aerosols. For this reason, we compare the KAZR increased detections with the
424 features (i.e. cloud and aerosol) detected by MPL above 3 km. It is obviously that ~~most~~
425 ~~of the~~ more than 90% of increased detections are also detected as features by MPL.
426 Below 3 km, we calculated the percentage by comparing the KAZR detections only
427 with the cloud pixels detected by MPL, since aerosol is always present in the lowest
428 several kilometers. To test whether those increased detections, which are not identified
429 as cloud by MPL under 3 km, are signal or noise, we examined the PDFs of MPL
430 normalized aerosol backscatter and depolarization corresponding to the KAZR
431 increased feature and KAZR noise regions in Figure 10a & 10b. The PDFs of MPL
432 backscatter for the KAZR feature and noise regions are quite different (Fig.10a) with
433 the mean backscatter of 0.15 for feature and 0.10 (*photoelectrons km⁻²*)/
434 ($\mu\text{s } \mu\text{J}^{-1}$) for noise. The mean of the MPL depolarization ratio is 0.16 for feature and
435 0.12 for noise although the PDFs are more similar (Fig.10b), because dust is the main
436 aerosol type over this region. We also plot the PDFs of KAZR SNR and LDR for its

437 feature and noise pixels (Figs. 10c and 10d), which are Gaussian-like for noise pixels,
438 very different from those for the increased detections. Table 2 shows the mean values
439 of the four quantities shown in Fig.10. All the differences of these mean values between
440 KAZR noise and increased feature regions pass the significant test at 95% confidence
441 level except for the MPL depolarization ratio. These increased features from our feature
442 mask could thus be dust (and/or some plankton) but not the false positive. Figure 9b
443 shows the profile of false negative (i.e. the percentage of the cloud pixels identified by
444 MPL but not by KAZR in the total MPL detected cloud pixels). We can see that our
445 method with the noise reduction has relative smaller false negatives especially in the
446 layers under 3 km and between 7 and 10 km. Table 3 is the confusion matrix of the
447 KAZR feature mask results from both our and old methods estimated by MPL cloud
448 feature. Overall, 70.7% cloud mask identified by MPL also recognized by the new
449 method, while this percent is 68.9% for the algorithm without noise reduction. The
450 difference of false positive between the two methods is only 0.1% as shown in table 3.
451 These numbers dose show an improvement of our method on recognize weak signals
452 by comparing with the results from the ARM MMCR method, however, they can not
453 be used to assess the accuracy of our method due to the MPL feature detection issue.

454 The percentage drops to a minimum of 70% at about 9 km, where the total increased
455 cloud range bins are only about 110 and there are 35 range bins that are identified by
456 our method not observed by MPL. Considering all the increased detections by our
457 method, 98.6% of them are confirmed by MPL as features.

458 5. Summary and Discussion

459 Based on image noise reduction technique, we propose a ~~new~~modified method to
460 detect hydrometeors from cloud radar return signals. The basic idea is to treat the SNR
461 value of each range gate as a pixel brightness and suppress the SNR distributions of
462 noise to a narrow range by convolving with a 2-D bilateral kernel which can effectively
463 avoid blurring the high frequency components (i.e. boundaries of a target).— After the
464 noise smoothing process, a special filter with central-pixel weighting scheme is used to
465 ~~get~~obtain the final cloud mask. The detection of the test square clouds shows that there
466 are two remarkable advantages of our method:— First the noise reduction scheme of our
467 algorithm can enhance the contrast between signal and noise, while keeping the cloud
468 boundaries preserved and detecting more hydrometeors with weak SNR values. Second
469 both false positive and failed negative rates for strong and moderate clouds can be
470 reduced to acceptably small values. A comparison of radar and lidar observed
471 ~~easeations~~ further highlight the advantage of our method on recognizing weak cloud
472 signal in application.—

473

474 *Acknowledgements:* This work was supported by the National Science Foundation of
475 China (41430425, 41575016, 41521004, 41505011), China 111 project (No.B 13045),
476 and the Fundamental Research Funds for the Central University (lzujbky-2016-k01).

477 Reference

478 Ackerman, T. P., and G. M. Stokes (2003), The Atmospheric Radiation Measurement
479 program (vol 56, pg 38, 2003), *Physics Today*, 56(2), 14-14.

480 Barker, H. W. (2000), Indirect aerosol forcing by homogeneous and inhomogeneous
481 clouds, *Journal of Climate*, 13(22), 4042-4049, doi:10.1175/1520-
482 0442(2000)013<4042:iafbha>2.0.co;2.

483 Barker, H. W., and Q. Fu (2000), Assessment and optimization of the gamma-weighted
484 two-stream approximation, *Journal of the Atmospheric Sciences*, 57(8), 1181-1188,
485 doi:10.1175/1520-0469(2000)057<1181:aaootg>2.0.co;2.

486 Bony, et al. (2015), Clouds, circulation and climate sensitivity, *Nature Geoscience*, 8(4),
487 261-268, doi:10.1038/ngeo2398.

488 Canny, J. (1986), A COMPUTATIONAL APPROACH TO EDGE-DETECTION, *Ieee*
489 *Transactions on Pattern Analysis and Machine Intelligence*, 8(6), 679-698.

490 Clothiaux, E. E., T. P. Ackerman, G. G. Mace, K. P. Moran, R. T. Marchand, M. A.
491 Miller, and B. E. Martner (2000), Objective determination of cloud heights and radar
492 reflectivities using a combination of active remote sensors at the ARM CART sites,
493 *Journal of Applied Meteorology*, 39(5), 645-665, doi:10.1175/1520-
494 0450(2000)039<0645:odocha>2.0.co;2.

495 Clothiaux, E. E., M. A. Miller, B. A. Albrecht, T. P. Ackerman, J. Verlinde, D. M. Babb,
496 R. M. Peters, and W. J. Syrett (1995), AN EVALUATION OF A 94-GHZ RADAR FOR
497 REMOTE-SENSING OF CLOUD PROPERTIES, *Journal of Atmospheric and*
498 *Oceanic Technology*, 12(2), 201-229, doi:10.1175/1520-

499 0426(1995)012<0201:aeoagr>2.0.co;2.

500 Clothiaux, E. E., K. P. Moran, B. E. Martner, T. P. Ackerman, G. G. Mace, T. Uttal, J.
501 H. Mather, K. B. Widener, M. A. Miller, and D. J. Rodriguez (1999), The atmospheric
502 radiation measurement program cloud radars: Operational modes, *Journal of*
503 *Atmospheric and Oceanic Technology*, 16(7), 819-827, doi:10.1175/1520-
504 0426(1999)016<0819:tarmpc>2.0.co;2.

505 Fu, Q., M. Baker, and D. L. Hartmann (2002), Tropical cirrus and water vapor: an
506 effective Earth infrared iris feedback?, *Atmospheric Chemistry and Physics*, 2, 31-37.

507 Fu, Q., B. Carlin, and G. Mace (2000a), Cirrus horizontal inhomogeneity and OLR bias,
508 *Geophysical Research Letters*, 27(20), 3341-3344, doi:10.1029/2000gl011944.

509 Fu, Q., M. C. Cribb, and H. W. Barker (2000b), Cloud geometry effects on atmospheric
510 solar absorption, *Journal of the Atmospheric Sciences*, 57(8), 1156-1168.

511 Fukao, S., and K. Hamazu (2014), Radar for Meteorological and Atmospheric
512 Observations, *Springer*.

513 He, K., J. Sun, and X. Tang (2013), Guided Image Filtering, *Ieee Transactions on*
514 *Pattern Analysis and Machine Intelligence*, 35(6), 1397-1409,
515 doi:10.1109/tpami.2012.213.

516 Hildebrand, P. H., and R. S. Sekhon (1974), Objective Determination of the Noise Level
517 in Doppler Spectra *Journal of Applied Meteorology*, 13, 808~811, doi:
518 [http://dx.doi.org/10.1175/1520-0450\(1974\)013<0808:ODOTNL>2.0.CO;2](http://dx.doi.org/10.1175/1520-0450(1974)013<0808:ODOTNL>2.0.CO;2).

519 Huang, J. P., J. Ge, and F. Weng (2007), Detection of Asia dust storms using multisensor
520 satellite measurements, *Remote Sensing of Environment*, 110(2), 186-191,

521 doi:10.1016/j.rse.2007.02.022.

522 Huang, J. P., P. Minnis, B. Lin, Y. H. Yi, T. F. Fan, S. Sun-Mack, and J. K. Ayers (2006a),
523 Determination of ice water path in ice-over-water cloud systems using combined
524 MODIS and AMSR-E measurements, *Geophysical Research Letters*, 33(21),
525 doi:10.1029/2006gl027038.

526 Huang, J. P., P. Minnis, B. Lin, Y. H. Yi, M. M. Khaiyer, R. F. Arduini, A. Fan, and G.
527 G. Mace (2005), Advanced retrievals of multilayered cloud properties using
528 multispectral measurements, *Journal of Geophysical Research-Atmospheres*, 110(D15),
529 doi:10.1029/2004jd005101.

530 Huang, J. P., Y. J. Wang, T. H. Wang, and Y. H. Yi (2006b), Dusty cloud radiative forcing
531 derived from satellite data for middle latitude regions of East Asia, *Progress in Natural
532 Science*, 16(10), 1084-1089.

533 Huang, J. P., et al. (2008), An Overview of the Semi-arid Climate and Environment
534 Research Observatory over the Loess Plateau, *Advances in Atmospheric Sciences*, 25(6),
535 906-921, doi:10.1007/s00376-008-0906-7.

536 Illingworth, A. J., et al. (2007), Cloudnet - Continuous evaluation of cloud profiles in
537 seven operational models using ground-based observations, *Bulletin of the American
538 Meteorological Society*, 88(6), 883+, doi:10.1175/bams-88-6-883.

539 King, M. D., S. Platnick, W. P. Menzel, S. A. Ackerman, and P. A. Hubanks (2013),
540 Spatial and Temporal Distribution of Clouds Observed by MODIS Onboard the Terra
541 and Aqua Satellites, *Ieee Transactions on Geoscience and Remote Sensing*, 51(7), 3826-
542 3852, doi:10.1109/tgrs.2012.2227333.

543 Kollias, E. E. Clothiaux, M. A. Miller, B. A. Albrecht, G. L. Stephens, and T. P.
544 Ackerman (2007a), Millimeter-wavelength radars - New frontier in atmospheric cloud
545 and precipitation research, *Bulletin of the American Meteorological Society*, 88(10),
546 1608+, doi:10.1175/bams-88-10-1608.

547 Kollias, E. E. Clothiaux, M. A. Miller, E. P. Luke, K. L. Johnson, K. P. Moran, K. B.
548 Widener, and B. A. Albrecht (2007b), The Atmospheric Radiation Measurement
549 Program cloud profiling radars: Second-generation sampling strategies, processing, and
550 cloud data products, *Journal of Atmospheric and Oceanic Technology*, 24(7), 1199-
551 1214, doi:10.1175/jtech2033.1.

552 Li, J., J. Huang, K. Stamnes, T. Wang, Q. Lv, and H. Jin (2015), A global survey of
553 cloud overlap based on CALIPSO and CloudSat measurements, *Atmospheric
554 Chemistry and Physics*, 15(1), 519-536, doi:10.5194/acp-15-519-2015.

555 Mace, G. G., T. P. Ackerman, P. Minnis, and D. F. Young (1998), Cirrus layer
556 microphysical properties derived from surface-based millimeter radar and infrared
557 interferometer data, *Journal of Geophysical Research-Atmospheres*, 103(D18), 23207-
558 23216, doi:10.1029/98jd02117.

559 Mace, G. G., E. E. Clothiaux, and T. P. Ackerman (2001), The composite characteristics
560 of cirrus clouds: Bulk properties revealed by one year of continuous cloud radar data,
561 *Journal of Climate*, 14(10), 2185-2203, doi:10.1175/1520-
562 0442(2001)014<2185:tccocc>2.0.co;2.

563 Marchand, R., G. G. Mace, T. Ackerman, and G. Stephens (2008), Hydrometeor
564 detection using Cloudsat - An earth-orbiting 94-GHz cloud radar, *Journal of*

565 *Atmospheric and Oceanic Technology*, 25(4), 519-533, doi:10.1175/2007jtecha1006.1.

566 Marr, D., and E. Hildreth (1980), THEORY OF EDGE-DETECTION, *Proceedings of*
567 *the Royal Society Series B-Biological Sciences*, 207(1167), 187-217,
568 doi:10.1098/rspb.1980.0020.

569 Perona, P., and J. Malik (1990), SCALE-SPACE AND EDGE-DETECTION USING
570 ANISOTROPIC DIFFUSION, *Ieee Transactions on Pattern Analysis and Machine*
571 *Intelligence*, 12(7), 629-639, doi:10.1109/34.56205.

572 Protat, A., D. Bouniol, J. Delanoe, P. T. May, A. Plana-Fattori, A. Hasson, E. O'Connor,
573 U. Goersdorf, and A. J. Heymsfield (2009), Assessment of Cloudsat Reflectivity
574 Measurements and Ice Cloud Properties Using Ground-Based and Airborne Cloud
575 Radar Observations, *Journal of Atmospheric and Oceanic Technology*, 26(9), 1717-
576 1741, doi:10.1175/2009jtecha1246.1.

577 Protat, A., J. Delanoe, P. T. May, J. Haynes, C. Jakob, E. O'Connor, M. Pope, and M. C.
578 Wheeler (2011), The variability of tropical ice cloud properties as a function of the
579 large-scale context from ground-based radar-lidar observations over Darwin, Australia,
580 *Atmospheric Chemistry and Physics*, 11(16), 8363-8384, doi:10.5194/acp-11-8363-
581 2011.

582 Ramanathan, V., R. D. Cess, E. F. Harrison, P. Minnis, B. R. Barkstrom, E. Ahmad, and
583 D. Hartmann (1989), CLOUD-RADIATIVE FORCING AND CLIMATE - RESULTS
584 FROM THE EARTH RADIATION BUDGET EXPERIMENT, *Science*, 243(4887), 57-
585 63, doi:10.1126/science.243.4887.57.

586 Randall, D. A., R.A. Wood, S. Bony, R. Colman, T. Fichefet, J. Fyfe, V. Kattsov, A.

587 Pitman, J. Shukla, J. Srinivasan, R.J. Stouffer, A. Sumi and K.E. Taylor (2007), Climate
588 Models and Their Evaluation. In: Climate Change 2007: The Physical Science Basis,
589 *Contribution of Working Group I to the Fourth Assessment Report of the*
590 *Intergovernmental Panel on Climate Change, [Solomon, S., D. Qin, M. Manning, Z.*
591 *Chen, M. Marquis, K.B. Averyt, M.Tignor and H.L. Miller (eds.)]. Cambridge*
592 *University Press, Cambridge, United Kingdom and New York, NY, USA.*

593 Sassen, K., and S. Benson (2001), A midlatitude cirrus cloud climatology from the
594 facility for atmospheric remote sensing. Part II: Microphysical properties derived from
595 lidar depolarization, *Journal of the Atmospheric Sciences*, 58(15), 2103-2112,
596 doi:10.1175/1520-0469(2001)058<2103:amcccf>2.0.co;2.

597 Stephens, G. L. (2005), Cloud feedbacks in the climate system: A critical review,
598 *Journal of Climate*, 18(2), 237-273, doi:10.1175/jcli-3243.1.

599 Stephens, G. L., et al. (2002), The cloudsat mission and the a-train - A new dimension
600 of space-based observations of clouds and precipitation, *Bulletin of the American*
601 *Meteorological Society*, 83(12), 1771-1790, doi:10.1175/bams-83-12-1771.

602 Su, J., J. Huang, Q. Fu, P. Minnis, J. Ge, and J. Bi (2008), Estimation of Asian dust
603 aerosol effect on cloud radiation forcing using Fu-Liou radiative model and CERES
604 measurements, *Atmospheric Chemistry and Physics*, 8(10), 2763-2771.

605 Thorsen, and Q. Fu (2015), Automated Retrieval of Cloud and Aerosol Properties from
606 the ARM Raman Lidar. Part II: Extinction, *Journal of Atmospheric and Oceanic*
607 *Technology*, 32(11), 1999-2023, doi:10.1175/jtech-d-14-00178.1.

608 Thorsen, Q. Fu, and J. Comstock (2011), Comparison of the CALIPSO satellite and

609 ground-based observations of cirrus clouds at the ARM TWP sites, *Journal of*
610 *Geophysical Research-Atmospheres*, 116, doi:10.1029/2011jd015970.

611 Thorsen; Fu, Q. N., Rob K.; Turner David D.; Comstock Jennifer M. (2015), Automated
612 Retrieval of Cloud and Aerosol Properties from the ARM Raman Lidar. Part I: Feature
613 Detection, *JOURNAL OF ATMOSPHERIC AND OCEANIC TECHNOLOGY*, 32(11),
614 1977-1998, doi:10.1175/JTECH-D-14-00150.1.

615 Tomasi, C., and R. Manduchi (1998), Bilateral Filtering for Gray and Color Images,
616 *IEEE International Conference on Computer Vision, Bombay, India*,
617 doi:10.1109/ICCV.1998.710815.

618 Wang, Z., and K. Sassen (2001), Cloud type and macrophysical property retrieval using
619 multiple remote sensors, *Journal of Applied Meteorology*, 40(10), 1665-1682,
620 doi:10.1175/1520-0450(2001)040<1665:ctampr>2.0.co;2.

621 Williams, K. D., and M. J. Webb (2009), A quantitative performance assessment of
622 cloud regimes in climate models, *Climate Dynamics*, 33(1), 141-157,
623 doi:10.1007/s00382-008-0443-1.

624 Yan, H. R., J. P. Huang, P. Minnis, Y. H. Yi, S. Sun-Mack, T. H. Wang, and T. Y.
625 Nakajima (2015), Comparison of CERES-MODIS cloud microphysical properties with
626 surface observations over Loess Plateau, *Journal of Quantitative Spectroscopy &*
627 *Radiative Transfer*, 153, 65-76, doi:10.1016/j.jqsrt.2014.09.009.

628 Yuan, J., Q. Fu, and N. McFarlane (2006), Tests and improvements of GCM cloud
629 parameterizations using the CCCMA SCM with the SHEBA data set, *Atmospheric*
630 *Research*, 82(1-2), 222-238, doi:10.1016/j.atmosres.2005.10.009. _____

Cloud Type	Performance (%)	Cloud Mask Confidence Level			
		≥10	≥20	≥30	≥40
Strong	False positive	0.048	0.044	0.009	0
	Failed negative	0.244	0.244	0.244	0.244
Moderate	False positive	0.103	0.103	0.063	0
	Failed negative	0.229	0.229	0.229	100
Weak	False positive	0.007	0.006	0.003	0
	Failed negative	9.774	96.788	100	100

631 Table 1. Summary of false positives and failed negatives for hypothetical strong,
632 moderate and weak cloud cases in Fig.4 a1, a2, and a3, respectively. _____

	<u>increased KAZR feature</u>	<u>KAZA noise</u>
<u>MPL backscatter</u>	<u>0.15</u>	<u>0.10</u>
<u>MPL depolarization ratio</u>	<u>0.16</u>	<u>0.12</u>
<u>KAZR SNR</u>	<u>3.9</u>	<u>0.1</u>
<u>KAZR LDR</u>	<u>-3.0</u>	<u>-0.4</u>

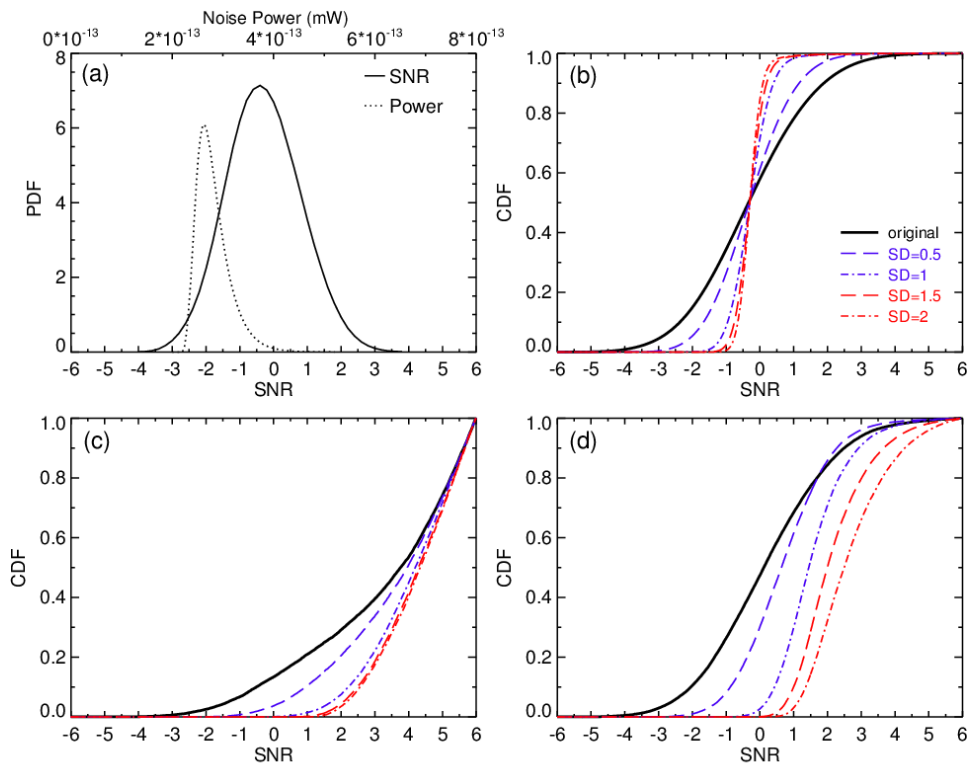
633

Table 2. Mean values of four quantities for KAZR increased feature and noise pixels

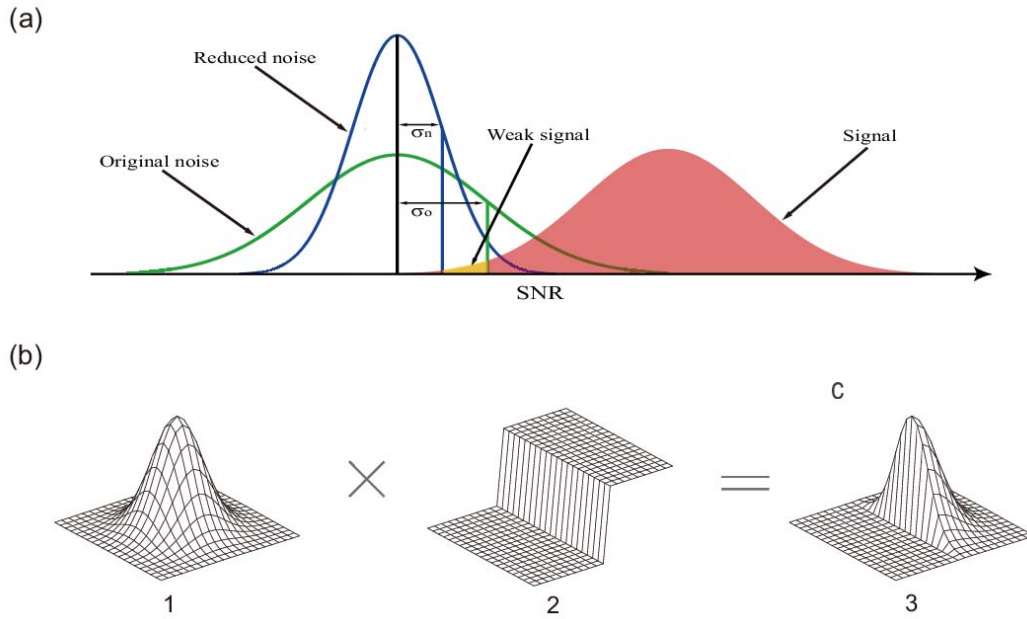
	<u>our method</u>	<u>MMCR method</u>
<u>True Positive</u>	<u>70.7%</u>	<u>68.9%</u>
<u>True Negative</u>	<u>95.4%</u>	<u>95.5%</u>
<u>False Positive</u>	<u>4.6%</u>	<u>4.5%</u>
<u>False Negative</u>	<u>29.3%</u>	<u>31.1%</u>

634 Table 3. Confusion matrix of KAZR mask results from our method and the ARM

635 MMCR algorithm estimated by MPL observations.

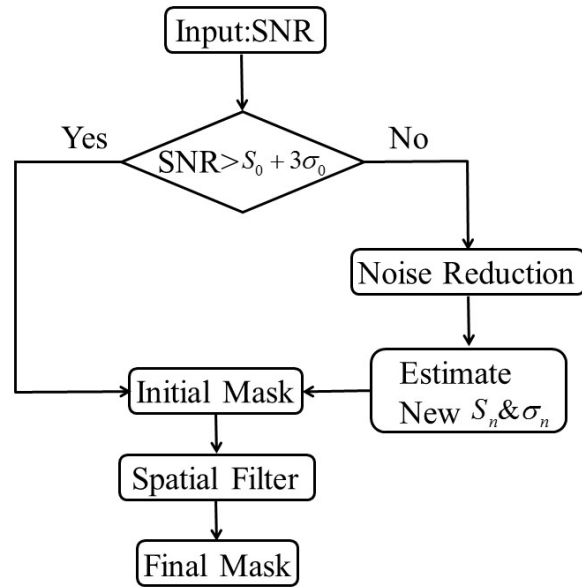


636 Figure 1. (a) Probability distribution function (PDF) of the noise power and SNR from
 637 the KAZR observations in a clear day of January 21, 2014. (b) Cumulative distribution
 638 function (CDF) of original and convolved SNR for the noise from the clear day. (c) and
 639 (d) CDF of original and convolved SNR from a cloudy case of January 4, 2014 for
 640 range gates inside and outside the cloud adjacent to the cloud boundary, respectively.
 641 The converted SNR is obtained by using a 2-D Gaussian distribution kernel (Eq. 2).

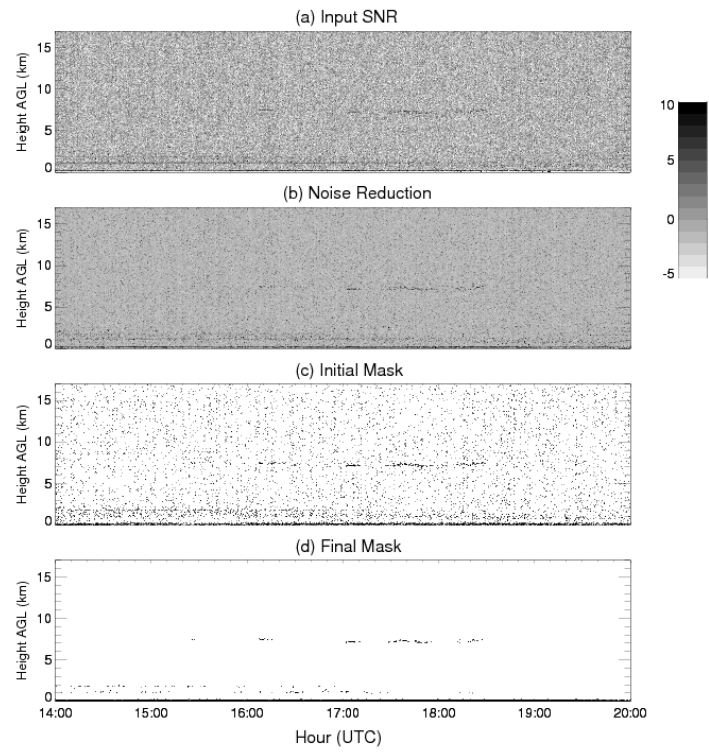


642 Figure 2. (a) comparison of original noise, reduced noise and hydrometeor signal
 643 distributions. σ_o and σ_n are one standard deviation of the original and reduced
 644 background noise, respectively. (b) Illustration of the bilateral filtering process. (b1)
 645 Gaussian kernel distribution in space. (b2) δ function. (b3) Bilateral kernel by
 646 combining Gaussian kernel with δ function.

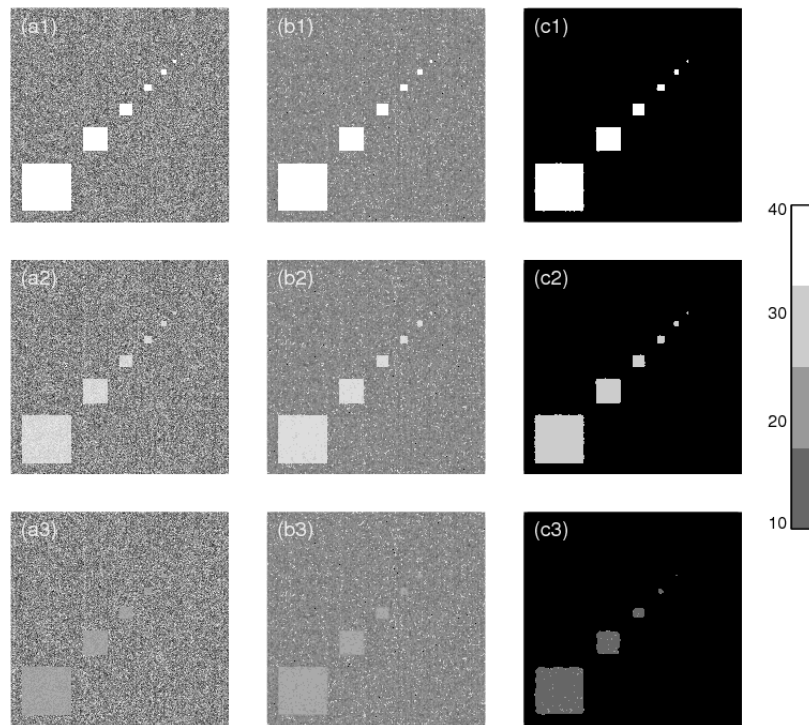
647



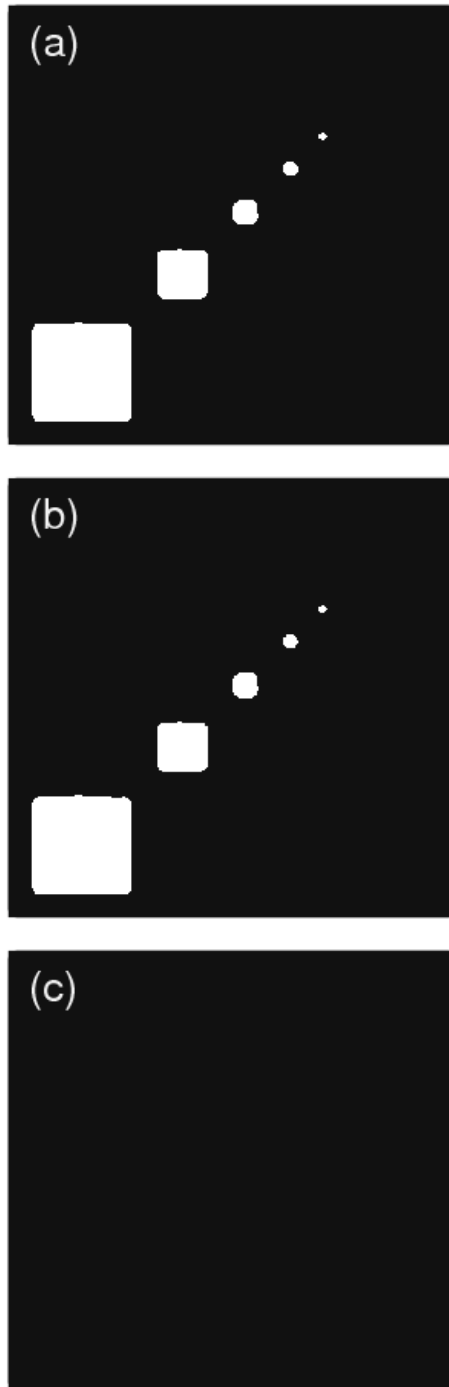
648 Figure 3. Schematic flow diagram for hydrometeor detection method. S_0 and S_n are
 649 the mean SNR for the original and reduced noise, respectively.



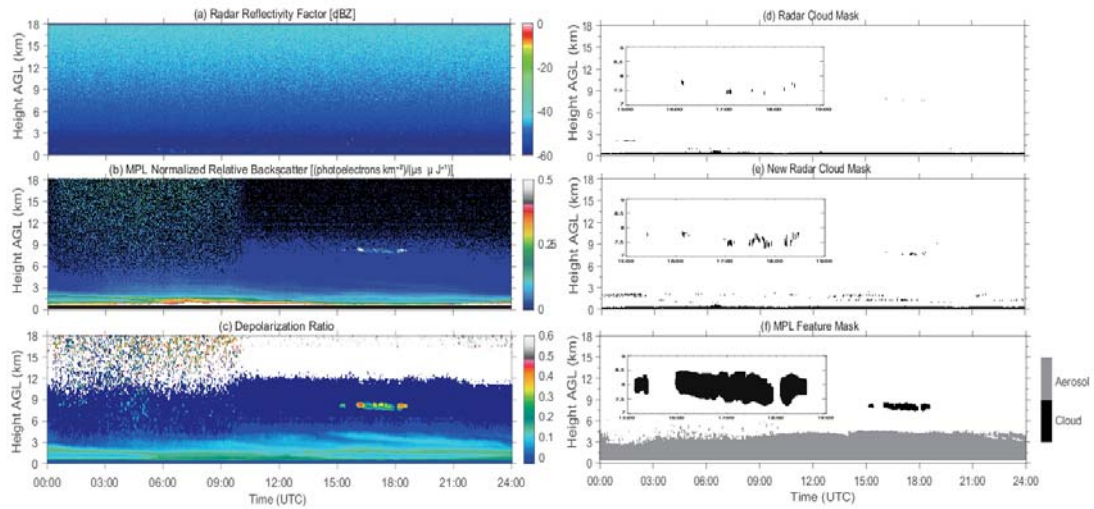
650 Figure 4. Illustration of the steps of the detection method using the real data of January
 651 8th, 2014.



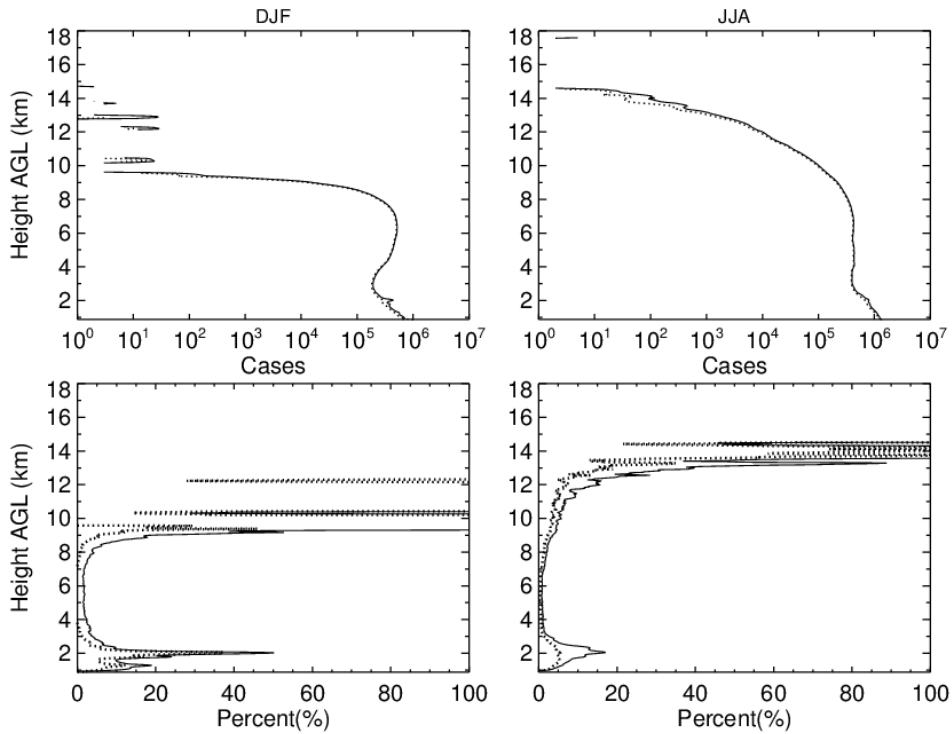
652 Figure 5. Panels a₁, a₂ and a₃ are three “square clouds” that have strong, moderate and
 653 weak SNR values with random Gaussian noise used to test the detection method. Panels
 654 b₁, b₂ and b₃ are SNR distributions after convolving the data with a bilateral kernel.
 655 Panels c₁, c₂ and c₃ are the final cloud mask filtered by the spatial filter.



656 Figure 6. Cloud mask without applying noise reduction and central pixel weighting. (a),
657 (b), (c) are for the targets with strong, moderate and weak SNR, respectively, from Fig.
658 4 a1, a2, and a3.

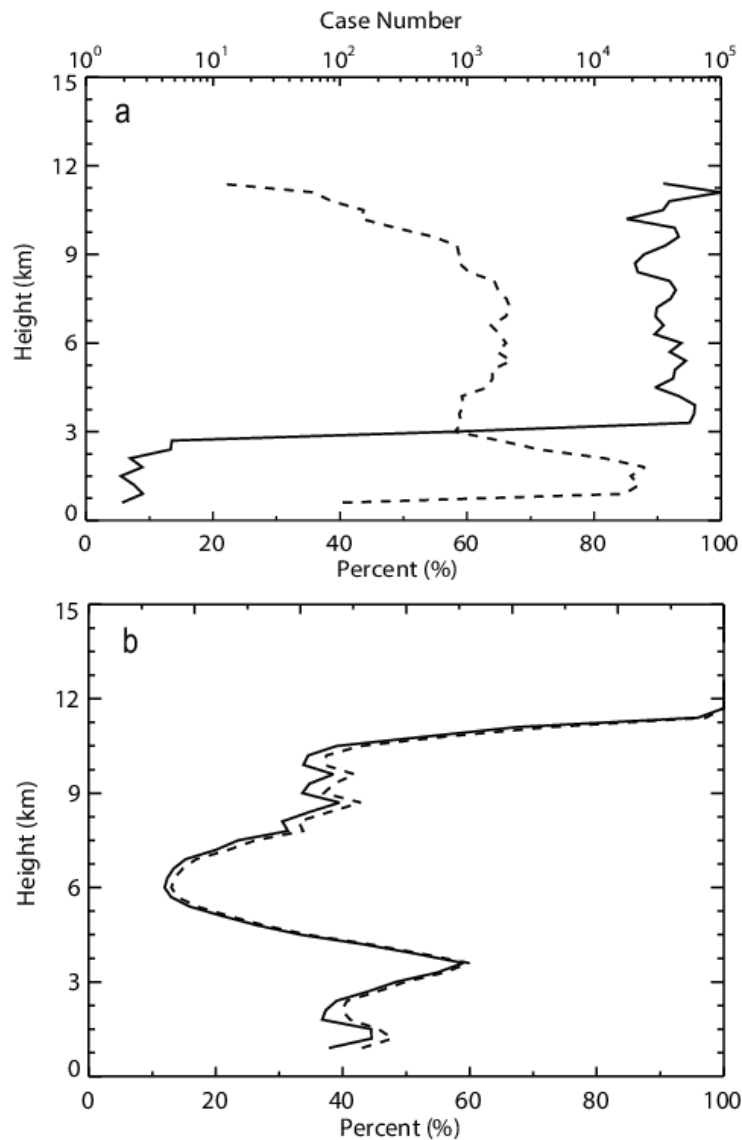


659 Figure 7. One-day example of radar- and lidar-observed cirrus cloud at the SACOL on
 660 January 8, 2014. (a) KAZR reflectivity. (b) MPL normalized backscatter intensity
 661 (c)MPL Depolarization Ration (d) radar cloud mask derived by the ARM ~~operational~~
 662 MMCR algorithm. (e) radar cloud mask derived by our new method. (f) MPL feature
 663 mask. Three windows in (d), (e), (f) show the zoom-in views of cirrus masks.

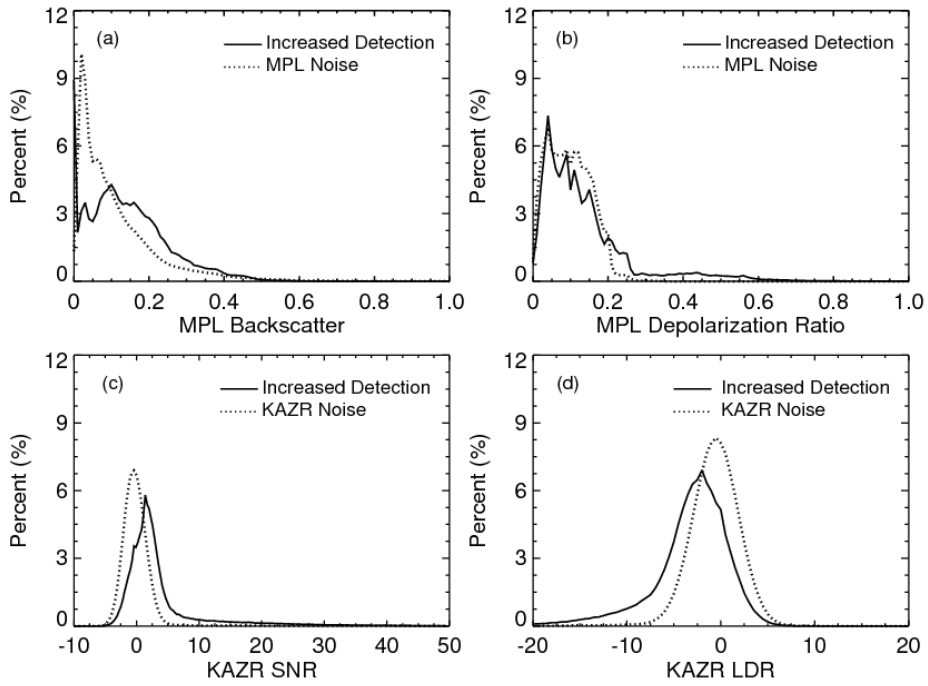


664 Figure 8. The upper panel shows the number of occurrences of the detected
 665 hydrometeor range bins from the two methods ~~with the confusion matrix~~. The solid line
 666 ~~is the number of range gates represents the results~~ derived from our ~~new~~ method. The
 667 dot line ~~represents the range gate number that are detected as signals by both methods~~.
 668 ~~The dashed line is the number of range gates detected as noise by our method but signal~~
 669 ~~by from the ARM MMCR algorithm. The dot-dash line is the increased range gates from~~
 670 ~~our method~~. The lower two panels demonstrate the increased percentage of
 671 hydrometeor bins from our ~~new~~ method comparing to the ARM MMCR
 672 ~~algorithm~~ ARM operational method. The solid line is calculated by applying both noise
 673 reduction and central-pixel weighting schemes, while the dashed line is calculated by
 674 only applying the central-pixel weighting scheme in our detection method.

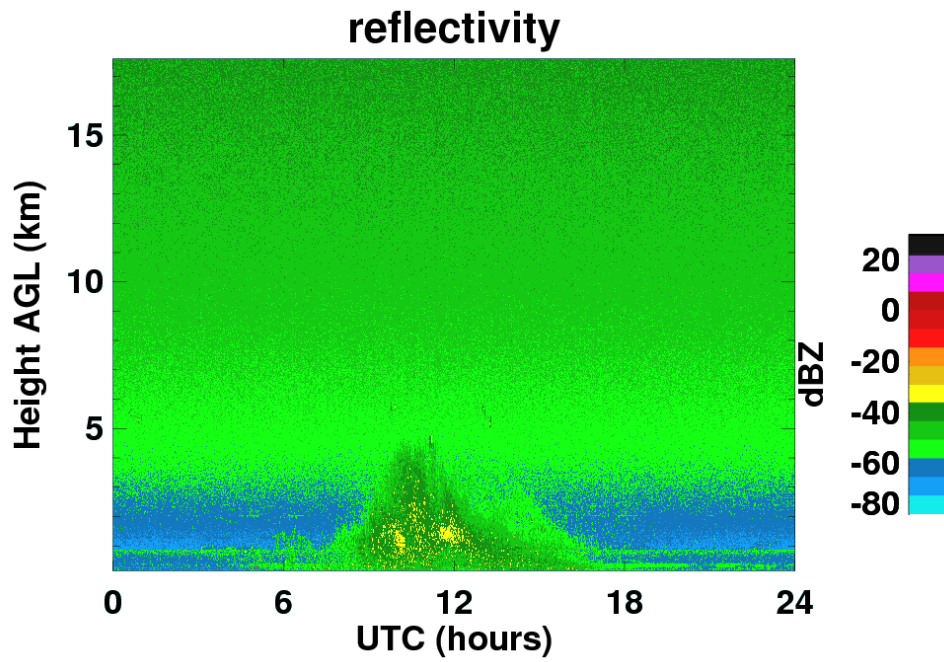
675



676 Figure 9. (a) A comparison of the increased detections with the MPL observations. (b)
 677 The percentage of the cloud pixels identified by MPL but not by KAZR in the total
 678 MPL detected cloud pixels. The solid line in Fig.9a is the percentage of increased
 679 detections seen by both KAZR with our method and MPL as compared with the total
 680 increased detections. The dot-dash line in Fig.9a is the number of increased detections.
 681 The solid lines in Fig. 9b represents for the algorithm with noise reduction step. The
 682 dash line in Fig. 9b is for the method without noise reduction scheme.



683 Figure 10. PDF of (a) MPL Backscatter, (b) MPL depolarization Ratio, (c) KAZR SNR
 684 and (d) KAZR LDR for the KAZR increased detections (solid line) and KAZR noise
 685 (dashed line) pixels.



686 Auxiliary Figure 1. KAZR reflectivity ~~A dust event observed~~ on January 29th, 2014 at
 687 the SACOL, indicating a dust event. The morphology and power level of the return
 688 signal is apparent not for a cloud from the surface to the height of 5 km between 0800
 689 to 1600 UTC.